

Vine Shoots-Derived Hard Carbons as Anodes for Sodium-Ion Batteries: Role of Annealing Temperature in Regulating Their Structure and Morphology

Darío Alvira,^{*[a, b]} Daniel Antorán,^[a, b] Mariano Vidal,^[c] Victor Sebastian,^[b, d, e, f] and Joan J. Manyà^{*[a, b]}

Sodium-ion batteries (SIBs) are considered one of the most promising large-scale and low-cost energy storage systems due to the abundance and low price of sodium. Herein, hard carbons from a sustainable biomass feedstock (vine shoots) were synthesized via a simple two-step carbonization process at different highest temperatures to be used as anodes in SIBs. The hard carbon produced at 1200 °C delivered the highest reversible capacity (270 mAh g⁻¹ at 0.03 A g⁻¹, with an acceptable initial coulombic efficiency of 71%) since a suitable balance between the pseudographitic domains growth and the retention of microporosity, defects, and functional groups was

achieved. A prominent cycling stability with a capacity retention of 97% over 315 cycles was also attained. Comprehensive characterization unraveled a three-stage sodium storage mechanism based on adsorption, intercalation, and filling of pores. A remarkable specific capacity underestimation of up to 38% was also found when a two-electrode half-cell configuration was employed to measure the rate performance. To avoid this systematic error caused by the counter/reference electrode polarization, we strongly recommend the use of a three-electrode setup or a full-cell configuration to correctly evaluate the anode response at moderate and high current rates.

[a] D. Alvira, D. Antorán, Prof. J. J. Manyà
Aragón Institute of Engineering Research (I3A)
Thermochemical Processes Group
University of Zaragoza, Escuela Politécnica Superior
Ctra. de Cuarte s/n, 22071 Huesca, Spain
E-mail: dalvira@unizar.es
joanjoma@unizar.es

[b] D. Alvira, D. Antorán, Prof. V. Sebastian, Prof. J. J. Manyà
Department of Chemical Engineering and Environmental Technologies
University of Zaragoza, Campus Río Ebro
María de Luna 3, 50018 Zaragoza, Spain

[c] Dr. M. Vidal
Department of Mechanical Engineering and Environmental Technologies
University of Zaragoza, Escuela Politécnica Superior
Ctra. de Cuarte s/n, 22071 Huesca, Spain

[d] Prof. V. Sebastian
Instituto de Nanociencia y Materiales de Aragón (INMA)
CSIC-Universidad de Zaragoza, Campus Río Ebro
Mariano Esquillor, s/n, 50018 Zaragoza, Spain

[e] Prof. V. Sebastian
Networking Research Center on Bioengineering Biomaterials and Nanomedicine
CIBER-BBN
28029 Madrid, Spain

[f] Prof. V. Sebastian
Laboratorio de Microscopías Avanzadas
Universidad de Zaragoza, Campus Río Ebro
Mariano Esquillor, s/n, 50018 Zaragoza, Spain

 Supporting information for this article is available on the WWW under
<https://doi.org/10.1002/batt.202300233>

 Part of Special Collection dedicated to Battery Research in Europe

 © 2023 The Authors. *Batteries & Supercaps* published by Wiley-VCH GmbH.
This is an open access article under the terms of the Creative Commons Attribution Non-Commercial NoDerivs License, which permits use and distribution in any medium, provided the original work is properly cited, the use is non-commercial and no modifications or adaptations are made.

Introduction

Sodium-ion batteries (SIBs) are called to lead the next generation of large-scale electrochemical energy storage systems required to support the grid integration of intermittent renewable sources.^[1] However, the design of high-performance anodes is one of the main bottlenecks to achieve the full potential of this technology.^[2] Since the electrochemical intercalation of Na⁺ into graphite is hampered due to thermodynamical issues,^[3] alternative anode materials to those commonly used in lithium-ion batteries need to be developed. In this context, hard carbons (HCs) with larger interlayer spacing than that of graphite are the most promising and widely investigated candidates, since they can store Na⁺ in their surface functionalities, defects, and pseudographitic domains.^[4,5]

Hard carbons derived from biomass waste resources (such as oatmeal, rice husk, sugarcane bagasse, banana peels, peanut shells, apple pomace, and corncob) received extensive attention due to superior reversible capacities as well as cost and sustainability considerations.^[6–12] The natural microstructure of biomass remains after carbonization, providing a large number of defects and pores together with randomly oriented pseudographitic domains.^[13] The inherent channels and pores create an interconnected 3D structure that improves the electrolyte penetration and provides more sodium pathways and ion buffering reservoirs.^[14] Moreover, some remaining heteroatoms (N, S, P, etc.) can provide more storage sites by direct electrochemically active covalent bonds or through the introduction of carbon vacancy defects that originate electron acceptor states.^[15]

In order to produce suitable anode materials for SIBs, biomass-derived hard carbons need to be tuned to adjust their key properties, namely the interlayer spacing, pore structure, and surface composition. An acid-washing treatment is also commonly required to remove biomass-inherent inorganic species (such as Mg, K, Ca, and Si), which can worsen the electrochemical performance of the active material by occupying active sites as well as giving rise to unwanted reactions.^[16] Nevertheless, the complexity and heterogeneity of biomass sources together with the lack of consensus concerning the sodium storage mechanism hinder a systematic strategy for the production of engineered HCs.^[17,18]

The selection of the biomass source plays a critical role since different precursors give rise to a wide range of hard carbons with diverse structural and chemical properties. Spheres,^[19] nanotubes,^[20] and 2D nanosheets^[21] have been obtained, although 3D hierarchical structures are the most commonly achieved. These 3D structures – derived from the intrinsic cell walls, plant channels, and pores – can result in the so-called honeycomb shape^[22,23] and provide pathways for fast Na⁺ transport in addition to buffer the electrode volume expansion/contraction during cycling.^[14] In terms of biomass constituents, decomposition of hemicelluloses and lignin leads to non-graphitic carbons, while the carbonization of cellulose results in more compact and highly crystalline carbon structures.^[7,24] Hence, a proper cellulose and hemicelluloses-lignin ratio is required to ensure enough ordered graphitic layers without an excessive degree of graphitization.^[25]

Concerning the sodium storage mechanism, three different Na⁺ storage processes have been documented in the literature: (i) adsorption on the surface edges and defects, (ii) intercalation between pseudographitic layers, and (iii) filling of nanopores. However, a consensus regarding the mechanisms governing sodium storage along the galvanostatic charge-discharge voltage profiles has not yet been reached; in this respect, six different models have been proposed: (i) insertion-filling model,^[26] (ii) adsorption-insertion model,^[27] (iii) three stage model,^[28] (iv) four stage model,^[29] (v) extended adsorption-insertion model,^[30] and (vi) adsorption-filling model.^[31] Despite this, there is a growing consensus that the high-voltage slope region and the low-voltage plateau are mainly caused by adsorption-driven storage and intercalation processes, respectively.^[32]

Regarding carbonization process conditions, higher peak or highest temperatures result in a greater extent of graphitization and lower interplanar distances. In consequence, and for a given biomass feedstock, there is an optimal temperature at which the maximum reversible capacity can be achieved, commonly between 1000 °C and 1400 °C.^[33] Porosity development is also crucial since pores can improve the charge-transfer kinetics, although high specific surface areas usually lead to the formation of thick solid electrolyte interphases (SEIs) and related low initial coulombic efficiency (ICE) values. Nonetheless, Zheng *et al.*^[34] stated that, in the case of HCs having a narrow microporous structure (i.e., pore sizes ≤ 1 nm), the SEI was very thin and hardly formed. Yang *et al.*^[35], for their part, reported that liquid electrolyte was unable to diffuse into

ultramicropores (pore sizes below 0.7 nm), which were only accessible to the bare Na ions. In view of the above, one can conclude that suitable HCs for SIB purposes would be those exhibiting a good balance among degree of graphitization, microporosity, and surface chemistry. Since all of these material features depend – to a higher or lesser extent – on the highest carbonization temperature, assessing its role for a given biomass feedstock is an essential step to guide further improvements.

Vine shoots are an agricultural waste with a high volume generation in wine-growing regions: 1.4–2.0 tons per hectare and year.^[36] Using vine shoots to produce a high value-added hard carbon would promote the valorization of this biowaste, being an additional source of income and also a CO₂ sequestration strategy. Herein, HCs were produced from vine shoots through a two-step carbonization process at a variety of high-temperature thermal treatments. The two-step carbonization process was selected because the intermediate char after the first step (namely pyrolysis) can be used as an organic amendment in agricultural soils (biochar).^[37] The development of advanced biochar-based materials gives rise to value-added products that can promote the production of this sustainable platform carbon material.^[38] The synthesized HCs were then tested as anodes in SIBs with the aim at establishing links between the measured electrochemical performance and the most important materials features, namely surface chemistry, degree of (pseudo)graphitization, and microporosity.

Experimental Section

Biomass feedstock

Vine shoots (*Vitis vinifera L.*) of the Cabernet Sauvignon variety was used as carbon precursor. The biomass was collected during winter pruning in a vineyard placed in the Somontano region (Aragon, Spain). Vine shoots with diameters between 8.5 and 15 mm were selected and then cut into smaller pieces of 4–7 cm in length. Proximate and elemental analyses, X-ray fluorescence (XRF) spectroscopy, and determination of the contents of main biomass constituents (i.e., hemicelluloses, cellulose, and lignin) were performed as stated in an earlier study.^[39]

Production of hard carbons

Vine shoots (VS) were carbonized through a two-step carbonization approach, as shown in Figure 1. Firstly, 300 g of vine shoots were pyrolyzed in a fixed-bed reactor under an inert N₂ atmosphere at an average heating rate of 5 °C min⁻¹. A scheme of the pyrolysis plant can also be found in Figure S1 (Supporting Information).

The pyrolysis peak temperature was 500 °C, with a soaking time of 60 min and a residence time of N₂ (carrier gas) within the reactor of 100 s. The obtained char, which was crushed and sieved to obtain particle sizes lower than 90 nm, was then washed with a HCl solution (2 mol dm⁻³), for 2 h at 50 °C, to extract inorganic elements and subsequently rinsed with distilled water until neutral pH was obtained. The unwashed and acid-washed intermediate VS-derived chars were named VS-500-UW and VS-500, respectively.

The VS-500 material (5 g per batch) was subjected to a second carbonization step at higher temperature. For this purpose, a



Figure 1. Graphical summary of the two-step carbonization process.

tubular ceramic reactor (made of mullite) inserted into a furnace (Carbolite TF1 16/60/300) was used. An argon atmosphere was kept to avoid the formation of nitrogen oxides (see Figure S2 for schematic layout). A heating ramp of $5\text{ }^{\circ}\text{C min}^{-1}$ and a soaking time of 2 h were applied at the tested highest carbonization temperatures (800, 1000, 1200, and 1400 °C). The resulting hard carbons were uniformly named as VS-x, where x refers to the highest carbonization temperature.

Characterization of Produced Hard Carbons

Morphological characterization was performed using an Inspect F50 A scanning electron microscope coupled with energy dispersive X-ray spectroscopy (SEM-EDX; FEI, The Netherlands) to analyze elemental composition on the surface of HCs. The structural analysis of produced HCs was further assessed by an Image Corrected Titan HR-TEM (FEI, The Netherlands) equipped with a SuperTwin® objective lens and a CETCOR Cs-objective corrector from CEOS Company, allowing a point-to-point resolution of 0.08 nm. The Titan microscope was operated at 90 kV. Digitalmicrograph® software was used to measure interplanar distances from HR-TEM images. X-ray photoelectron spectroscopy (XPS; AXIS Supra instrument from Kratos Analytical Ltd, UK) was applied to identify the oxygen- and nitrogen-containing functional groups on surface from deconvolution of the C 1s and N 1s regions, respectively.

Structural characterization was performed using X-ray powder diffraction (XRD; Empyrean instrument from Malvern Panalytical, UK, $\lambda=0.154$ nm) and Raman spectroscopy (Alpha 300 model from WITec, Germany, $\lambda=532$ nm). The interlayer space between graphene layers (d_{002}), the apparent crystallite thickness along the c-axis (L_c), the apparent crystallite width along the a-axis (L_a), and the number of graphene stacking layers (n) were calculated from the XRD spectra using the Bragg and Scherrer equations, as illustrated in our previous article.^[40] The Raman spectra, which were collected at three different locations for each sample, were deconvoluted into one Gaussian-shaped band (D3) and four Lorentzian-shaped bands (G, D1, D2, and D4) in triplicate to calculate the $A_{\text{D}_1}/A_{\text{G}}$ ratio and L_a .^[41]

The micro- and ultra-microporosity of HCs were estimated from CO_2 adsorption isotherms at 273 K (using an Autosorb-iQ analyzer from Quantachrome, Anton Paar, Germany) once the samples were outgassed at 150 °C for 8 h under vacuum. The Brunauer-Emmett-Teller (BET) model was adopted to calculate the specific surface

area while the pore size distribution was determined using a Non-Local Density Functional Theory (NLDFT) model.

Electrochemical characterization

The electrochemical performance of active materials was evaluated using a three-electrode Swagelok t-cell prototype that was designed to contain circular electrodes (12 mm diameter) under a constant pressure of 0.2 N mm^{-2} (see Figure S3a). The plugs were made of stainless steel AISI 316-L and a high-density polyethylene tube was used to host the electrodes. When two-electrode measurements were carried out, a plug was used to close the central port of the Swagelok t-case (see Figure S3b). Working electrodes were prepared by mixing the produced HC with acetylene black (as conductive agent) and styrene-butadiene rubber (SBR) and carboxymethyl cellulose (CMC) (as binder compounds) at a mass ratio of 80:10:5:5. A homogeneous slurry was obtained by adding DI water with vortex agitation. Then the slurry was coated on an aluminum current collector (16 mm thickness) using a baker applicator to obtain a thickness-controlled composite electrode (100 µm) with a final mass loading of 2.36 mg cm^{-2} . Lastly, the electrodes were punched and dried under vacuum at 120 °C overnight.

A sodium metal disc (12 mm diameter) was used as counter electrode (CE) and reference electrode (RE) in the two-electrode setup, while an additional disc of metal sodium (5 mm diameter) was used as RE in the three-electrode cell. The separator between the working and counter electrodes was made of 190 mm thick glass fiber filter. The electrolyte, which was supplied by Solvionic (France), was composed of a NaTFSI solution (1 mol dm^{-3}) in a mixture (1:1 vol.) of dimethyl carbonate (DMC) and ethylene carbonate (EC) as solvent (60 ml of electrolyte were applied to the cell). The Swagelok cells were assembled in an argon-filled glovebox (H_2O and O_2 contents below 0.5 ppm) from MBraun (Germany).

Electrochemical measurements were conducted using SP-200 potentiostats (Bio-Logic, France) in a temperature range between 19 and 22 °C. The galvanostatic charge/discharge (GCD) cycles were performed within a potential window of 0.01–2.5 V (vs. Na/Na^+), whereas the cyclic voltammetry profiles were collected at a scan rate of 0.1 mV s^{-1} between cut-off voltages of 0.01 and 2.5 V. Galvanostatic intermittent titration (GITT) measurements were performed at a current density of 30 mA g^{-1} , a pulse time of 20 min, and relaxation periods of 1 h at open circuit.

Results and Discussion

Features of the biomass source

The electrochemical performance of plant-derived HCs is strongly influenced by the morphology and the physicochemical properties of the precursor.^[42] A lignin-rich precursor containing above 25 wt.% has been suggested to guarantee enough ordered graphitic layers and good electron conductivity, while avoiding an excessive graphitization.^[42–44] Furthermore, low ash contents are required, since inorganic elements (e.g., Mg, Ca, K, and Si) can occupy some sodium storage active sites and trigger parasitic reactions during sodiation.^[45] Based on the above, VS biomass has a lignin content of 20.3 wt.% (which is relatively high for a lignocellulosic material but lower than the suggested 25 wt.% threshold); however, its low ash content (1.08 wt.%) is certainly appropriate for electrochemical energy storage applications. In addition, the HCl-washing step after pyrolysis is justified by the relatively high contents of Ca, K, and Mg in the VS ash, as shown in Table 1.

Physicochemical characterization

After the first carbonization at 500 °C, and as deduced from the SEM images shown in Figure 2, the resulting VS-500 carbon material retained the raw plant tissue microstructure (see SEM images for pristine VS in Figure S4). This fact can facilitate the electrolyte penetration and Na⁺ diffusion. Porous Swiss cheese-like and 2D walls can be seen in Figure 2(a–c). Moreover, as the carbonization temperature increased to 1000 and 1400 °C, these biomass structures still remained, as shown in Figures 2(d and e). At the highest temperature, a morphological change can also be observed in the form of surface roughness (see Figure 2f), probably due to volatiles release and rearrangement phenomena.^[46]

On the other hand, the HRTEM images presented in Figure 3 provide valuable information on the degree of ordering and the growth of the pseudographitic domains during the thermal annealing. VS-500 exhibited an amorphous and disordered structure, without observing clear patterns or pseudographitic domains. When the temperature raised to 800 and 1000 °C (Figure 3b and c), an increasing formation of pseudographitic domains with randomly oriented stripes was observed, as well as the presence of a certain mesoporosity. Some interlayer distances (d_{002}) were determined from the HR-TEM images and were found to be higher than 0.37 nm, therefore suitable for accommodating sodium ions through the insertion/desertion mechanism. Several values of d_{002} were even higher than 0.40 nm, enabling pseudoadsorption of Na⁺ according to the extended adsorption-insertion model.^[30]

After heating up to 1200 °C, a full ordered pseudographitic HC with interlayer distances between 0.37 and 0.40 nm was obtained (see Figure 3d). Small graphitic domains ($d_{002} = 0.336$ nm) in the carbon edges were also found (as shown in Figure 3e). The increasing structural ordering with temperature, promoted by strong van der Waals interaction between

Table 1. Results from biomass constituents, proximate, ultimate, and ash composition analysis of vine shoots.

Lignocellulosic constituents and extractives [wt.% in dry basis]	
Hemicelluloses	24.8 ± 1.6
Cellulose	34.2 ± 1.9
Lignin	20.3 ± 1.4
Extractives	4.54 ± 0.37
Proximate analysis [wt. %]	
Moisture	7.97 ± 0.68
Ash (dry basis)	1.08 ± 0.05
Volatile matter (dry basis)	74.0 ± 1.19
Fixed carbon (dry basis)	24.9 ± 1.91
Ultimate analysis [wt.% in daf basis]	
C	47.1 ± 0.14
H	5.29 ± 0.09
N	0.66 ± 0.05
O (by difference)	47.0
Inorganic matter as equivalent oxides [wt.% of ash]	
CaO	58.3 ± 0.25
K ₂ O	18.4 ± 0.12
MgO	6.66 ± 0.14
SiO ₂	5.73 ± 0.08
Fe ₂ O ₃	3.51 ± 0.11
Al ₂ O ₃	2.57 ± 0.07
P ₂ O ₅	1.24 ± 0.04
PbO	0.26 ± 0.02
S (inorganic)	0.60 ± 0.03
Cl (inorganic)	0.48 ± 0.02
MnO	0.53 ± 0.03
ZnO	0.32 ± 0.02
SnO ₂	0.26 ± 0.02
TiO ₂	0.34 ± 0.02
CuO	0.09 ± 0.01

adjacent graphene layers, could enhance the electronic conductivity of produced HCs, resulting in improved electrode materials.^[47] When the carbonization temperature was further increased to 1400 °C, more of these full graphitized domains appeared (see Figure 3f). In spite of the expected improvement in conductivity, the smaller interlayer distances of these domains could hinder the intercalation of sodium ions, leading to a decrease in the availability of storage active sites.^[48] Fast Fourier transform patterns (given in Figure S5) also corroborated the increasing ordering and degree of graphitization with an increasing carbonization temperature by showing more well-defined diffraction rings.

With regard to XRD results, Figure 4(a) shows the patterns obtained for the VS-derived HCs. Table 2 reports the parameters obtained using the Bragg and Scherrer equations, which seem to be in agreement with the results from both SEM and HR-TEM images. As can be deduced from Table 2, an increase in the

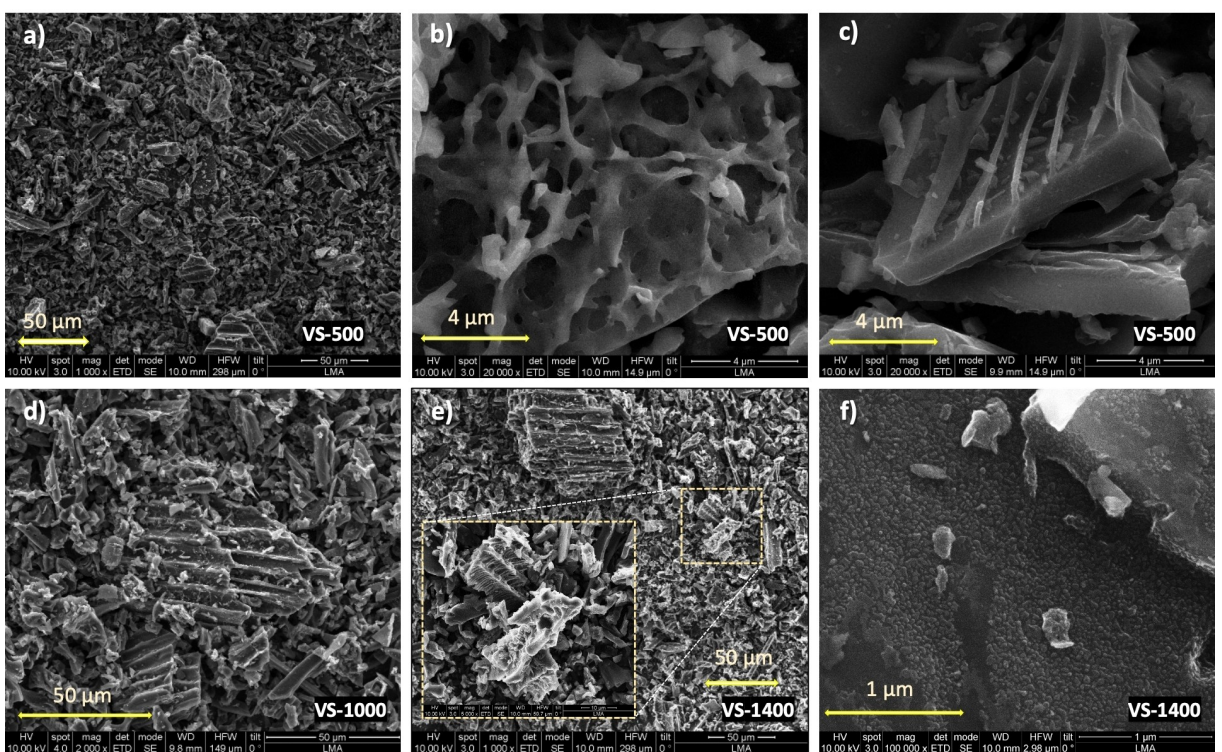


Figure 2. SEM images of a–c) VS-500, d) VS-1000, and e and f) VS-1400 carbons.

Table 2. Structural characteristics of HCs from XRD and Raman analyses.

	From XRD			From Raman		
	d_{002} [nm]	L_c [nm]	L_a [nm]	n	A_{D1}/A_G	L_a [nm]
VS-800	0.382	0.892	2.573	2.338	7.458 ± 0.152	2.598 ± 0.053
VS-1000	0.379	0.886	2.991	2.338	5.291 ± 0.075	3.661 ± 0.051
VS-1200	0.377	1.026	3.789	2.723	4.185 ± 0.147	4.632 ± 0.165
VS-1400	0.372	1.129	4.110	3.035	3.384 ± 0.086	5.727 ± 0.146

highest carbonization temperature led to higher degrees of graphitization, with a gradual increase in the lengths of the pseudographitic domains as well as in the number of stacked graphitic layers. In addition, a slight decrease in the average interlayer distance was observed, although the lowest d_{002} value still remained above the minimum value for sodium intercalation (0.36 nm). Figure 4(b), for its part, displays the Raman spectra for a given sample (VS-1200; see the rest of spectra in Figure S.6), whereas Table 2 reports the A_{D1}/A_G ratios and L_a values. The progressive decrease in the A_{D1}/A_G ratio (from 7.458 for VS-800 to 3.384 for VS-1400) is also consistent with the previous findings. Since the deconvoluted D1 band (ca. 1350 cm^{-1}) and G band (ca. 1590 cm^{-1}) are assigned to amorphous carbon domains and graphite-containing carbons, respectively, a lower A_{D1}/A_G ratio can be ascribed to a higher ordering of carbon structure.

From Figure 4(c) and Table 3, which displays the CO_2 adsorption isotherms at 0°C and the textural features deduced from them, respectively, it can be deduced a sudden increase in microporosity when the second carbonization step took place at 800°C , probably due to the decomposition of some unreacted biomass polymers (mainly lignin derivates) and the subsequent release of small hydrocarbon molecules.^[49,50] However, when the highest temperature was gradually increased, a slight decrease in ultra/microporosity was first observed for the VS-1000 sample, followed by a loss of practically all the ultra/microporosity for the VS-1200 HC, and a nondetectable surface area for the VS-1400 carbon. The loss of microporosity for the last two HCs could be explained by the fact that thermal annealing at higher temperatures induce graphene layer organization (i.e., ordering), resulting in the shrinkage of narrow micropores.^[51,52] At higher enough temperatures, the carbon

Table 3. Surface areas and micropore volumes of the HCs deduced from CO_2 adsorption isotherms.

	Surface area BET [$\text{m}^2\text{ g}^{-1}$]	Surface area NLDFT [$\text{m}^2\text{ g}^{-1}$]	Pore volume NLDFT [$\text{cm}^3\text{ g}^{-1}$]
VS-500	101	85.4	0.031
VS-800	154	140	0.047
VS-1000	130	85.2	0.036
VS-1200	3.13	0.387	1.6×10^{-4}
VS-1400	–	–	–
VS-1200-UW	6.05	2.20	1.0×10^{-3}

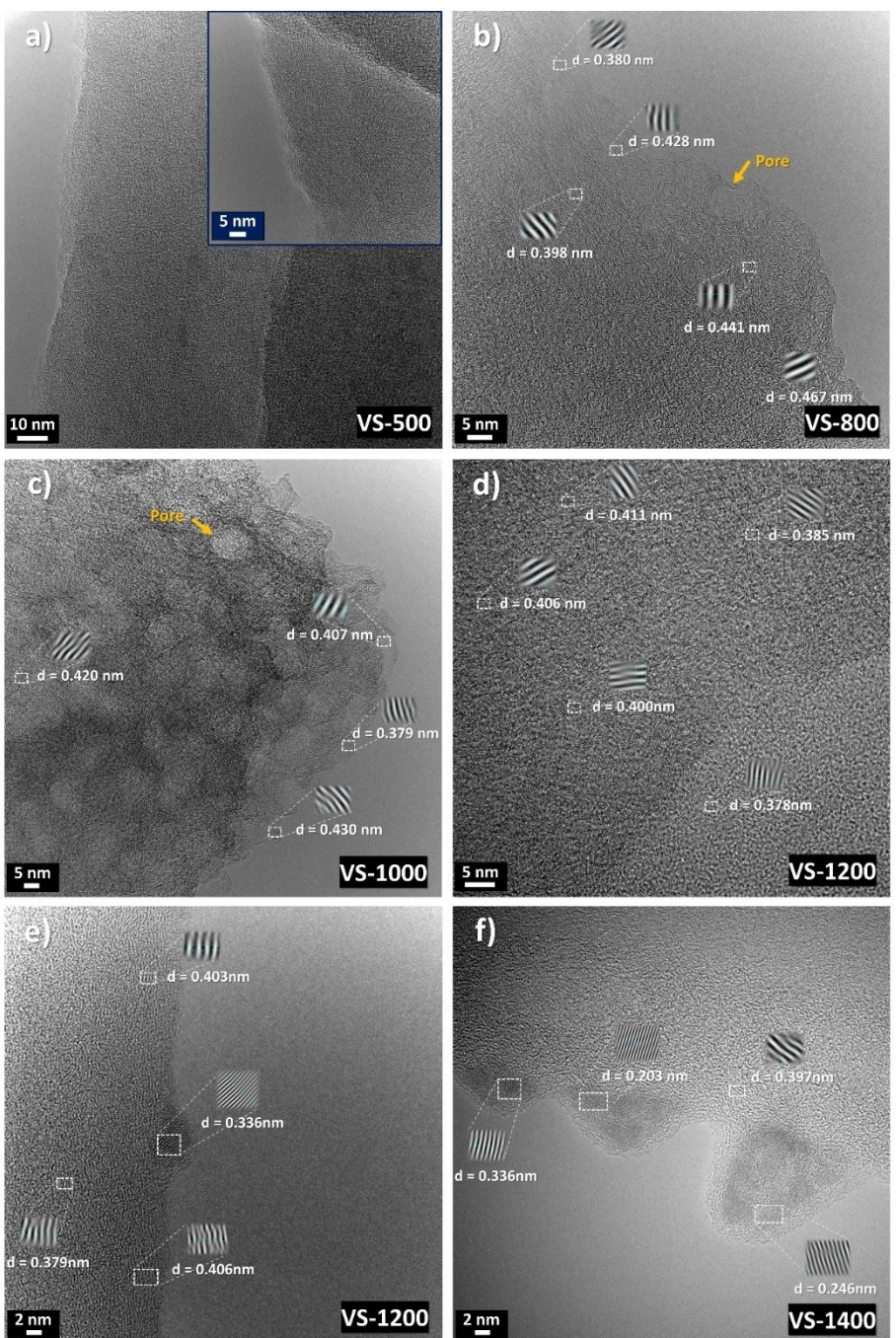


Figure 3. HR-TEM images of a) VS-500, b) VS-800, c) VS-1000, d) e) VS-1200, and f) VS-1400 carbons.

can also undergo plastic transformations due to melting and sintering processes, leading to additional pore closing and smooth and compact surfaces.^[53] The pore size distribution plots and pore volume histograms are available in Figures S7 and S8, respectively. As can be observed from both figures, the VS-500 HC exhibited a bimodal pore size distribution, with a first peak at ca. 0.6 nm (ultramicropore region) and a second one at ca. 0.8 nm (narrow micropore region). Regarding the VS-800 sample, it also exhibited a bimodal distribution, with higher contribution from ultramicropores smaller than 0.6 nm. Finally,

a certain pore widening (from narrow ultramicropores to micropores) was observed for the VS-1000 HC.

Concerning the elemental composition on surface of HCs, Figure 4(d) shows the results from the EDX mapping measurements (the related spectra are available in Figures S9–S13), which clearly indicate that the HCl-washing treatment allowed to remove almost all the calcium, potassium, and magnesium contained in the raw char (VS-500-UW). A gradual decrease in the amount of oxygen with the increasing highest carbonization temperature was also observed, from 12.36% (VS-500) to 3.16% (VS-1400) (see Table S1 for more details). This finding

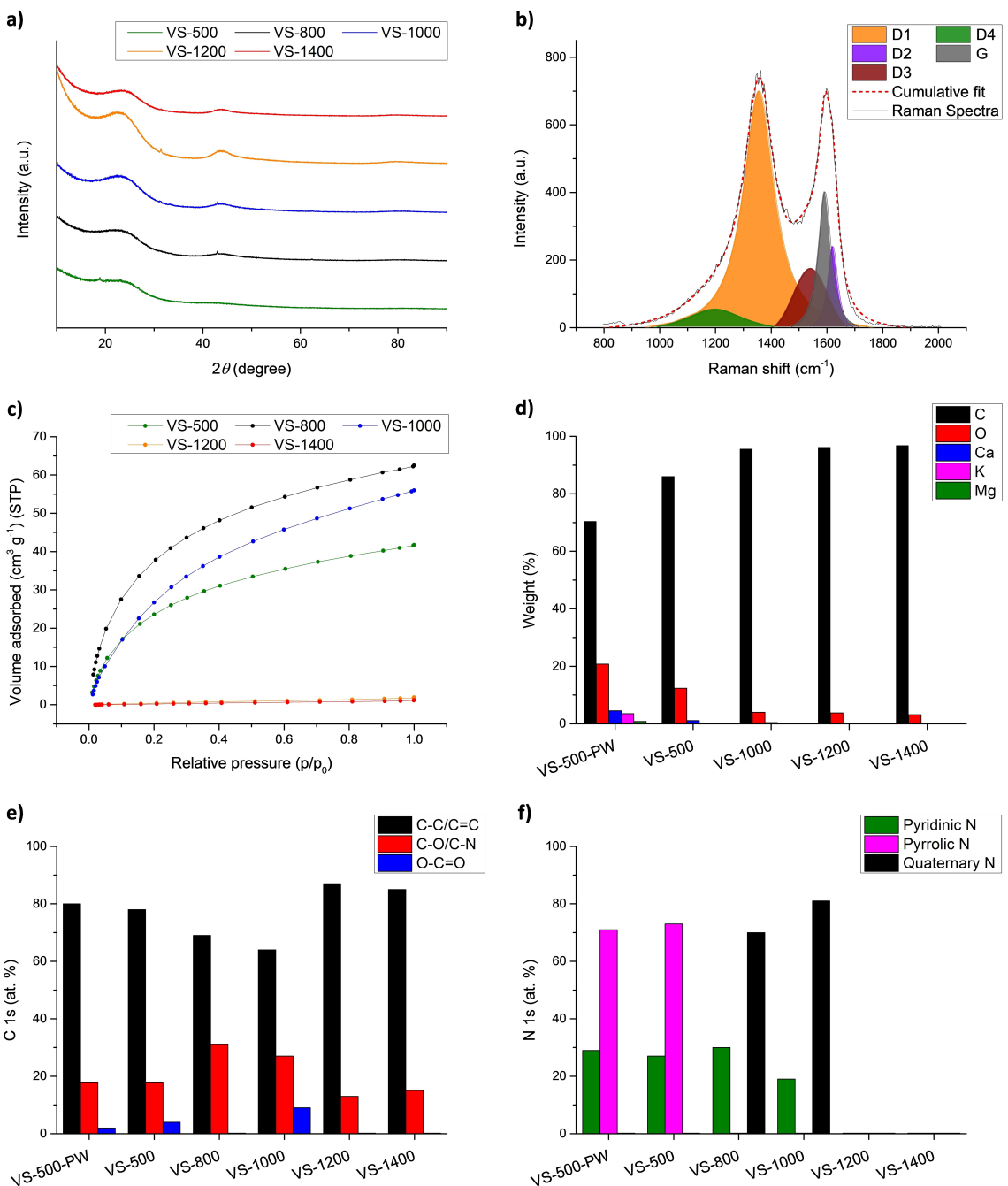


Figure 4. a) XRD patterns, b) Raman spectra deconvolution for the VS-1200 sample, c) CO_2 adsorption isotherms at 0°C , d) elemental composition from EDX, and results from deconvolution of XPS spectra for e) C 1s and f) N 1s regions.

is consistent with the expected progressive loss of O-containing functional groups on surface. Nevertheless, results from XPS measurements (see Table S2 for estimated quantification of peaks), did not fully agree with the above-mentioned EDX elemental mapping results. From the deconvoluted spectra for high-resolution XPS C 1s regions given in Figure S14 (see also Figure 4e), it can be seen that the area of the peak attributed to C–O/C–N bonds reached its maximum value for the VS-800 HC. The unexpected lower area obtained for the same peak for the intermediate char (VS-500) could be ascribed to the deposition

of secondary char (from volatiles recondensation or repolymerization, with low oxygen content) on the surface of the nascent char during pyrolysis. Regarding the nitrogen-containing groups, Figures 4(f) and S15 clearly show the transformation of pyrrolic and pyridinic N into more stable quaternary N when the highest carbonization temperature increased from 800 to 1000°C .^[54] For higher carbonization temperatures (i.e., 1200 and 1400°C), no N-containing surface groups were detected. The absence of pyrrolic and/or pyridinic N-containing moieties can result in lower slope capacity contributions, since they can

enhance the reversible adsorption of Na ions due to their electron deficient nature.^[55,56]

Electrochemical performance

The acquired cyclic voltammetry (CV) curves for the first three discharge/charge cycles are shown in Figure 5. The pair of sharply redox peaks appearing ca. 0.01 and 0.2 V (for HCs) can be mainly attributed to the reversible insertion/extraction of Na ions, respectively,^[29] although filling of pores with Na ions could also take place in this voltage range. As expected from the physicochemical characterization results, no intercalation-deintercalation processes were discernable for the VS-500 intermediate char, due to an insufficient degree of graphitization

(and related poor conductivity). The current response occurring at higher voltages is generally attributed to pseudocapacitive phenomena on surface (i.e., slope region). On the other hand, a broad peak was observed between 0.1 and 1 V in all the samples during the first discharge (cathodic current). This can be ascribed to SEI formation as well as to irreversible adsorption of Na⁺ in defects and functional groups.^[57] This irreversible capacity gradually decreased with increasing carbonization temperature (see dotted area in Figure 5), probably due to a lesser extent of irreversible adsorption of Na ions on surface functionalities. The almost overlapped CV profiles measured for the 2nd and 3rd cycles also reveal the stability of the formed SEI layer and high-capacity retention of the HC-based anodes.

Figure 6 shows the first 5 galvanostatic discharge/charge cycles at an intensity of 0.03 A g⁻¹ for all the produced HCs. The

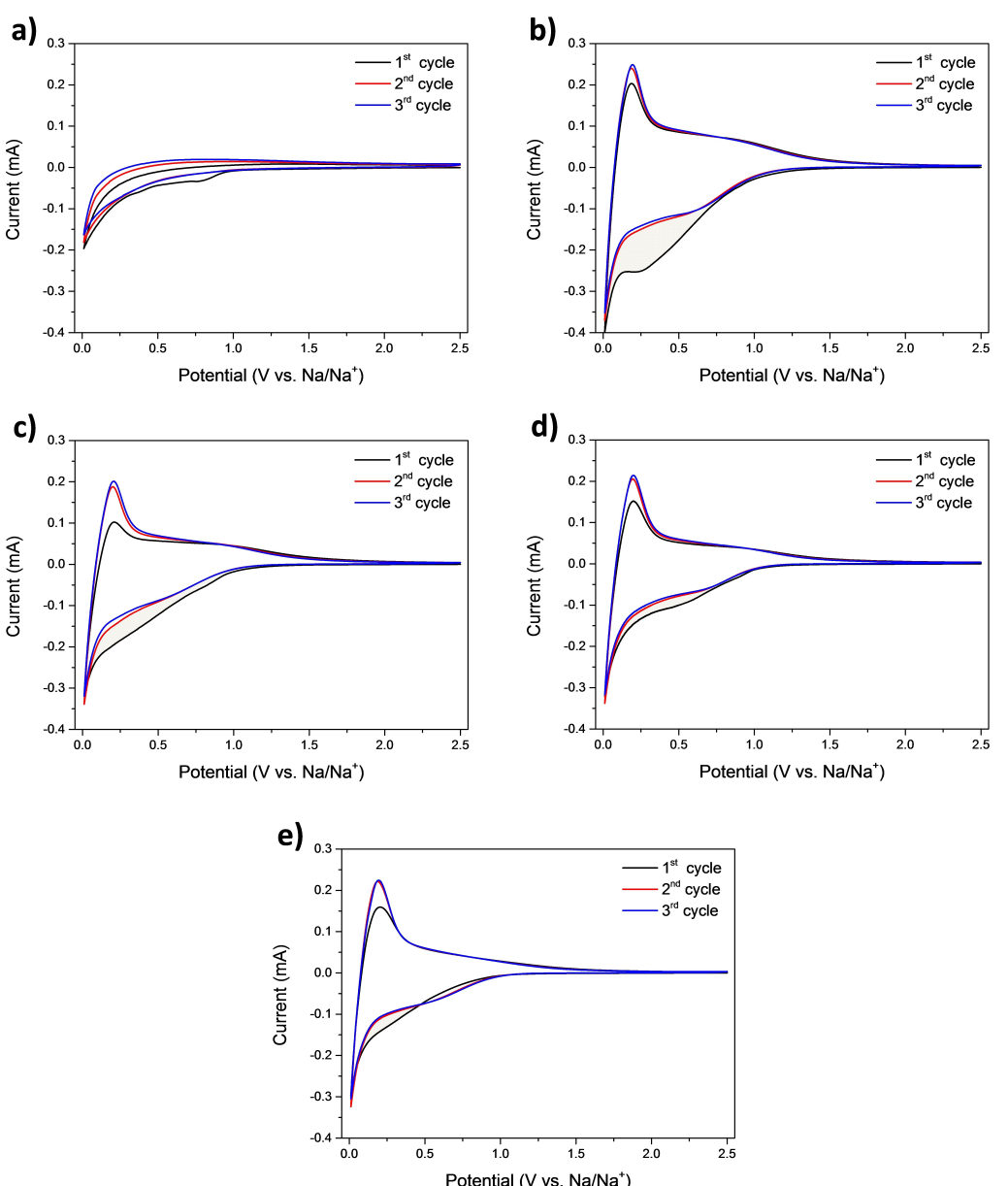


Figure 5. CV curves of the first three cycles for a) VS-500, b) VS-800, c) VS-1000, d) VS-1200, and e) VS-1400.

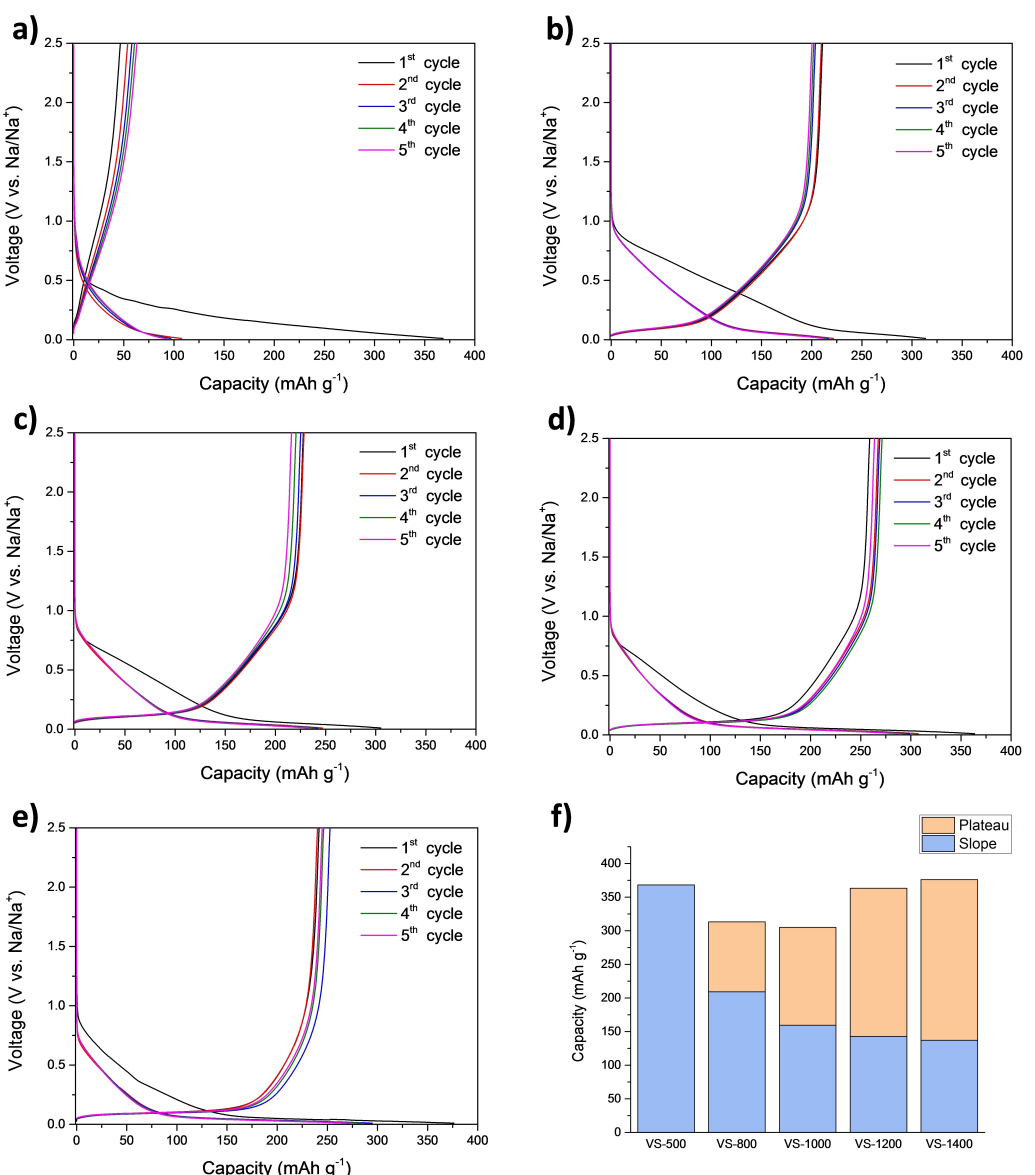


Figure 6. Galvanostatic dis/charge profiles at a current rate of 0.03 A g^{-1} for a) VS-500, b) VS-800, c) VS-1000, d) VS-1200, and e) VS-1400. f) Plateau and slope region contribution during the 1st sodiation.

aforementioned two voltage regions are observed: a plateau region from *ca.* 0.01 to *ca.* 0.1 V (mostly associated with intercalation processes) and the slope region from 0.1 to 2.5 V (related to faster surface phenomena). In consonance with the CV results, VS-500 shows the worse capacity values ($\sim 50 \text{ mAh g}^{-1}$) and no plateau region contribution. Moreover, the low ICE observed (12.7%) was explained by the irreversible adsorption of Na ions on surface during the first discharge process.

Among all the synthesized HCs, VS-1200 exhibited the best sodium storage performance at 0.03 A g^{-1} , with first discharge and charge capacities of 363.4 and 258.9 mAh g^{-1} , respectively (ICE of 71.2%). This good performance can be the result of a proper balance among degree of graphitization, functional groups available on surface, and prevalence of some narrow micropores. The plateau and slope capacity contributions during the first discharge are shown in Figure 6(f). The observed

gradual increase in the plateau contribution (intercalation processes in the low voltage range) with the increasing carbonization temperature is consistent with the higher degree of pseudographitization of high-temperature HCs. Likewise, the decrease in the slope contribution with the increasing carbonization temperature (and the related loss of functional groups on surface) also confirms the pseudocapacitive nature of the sodium storage processes taking place in this voltage region. Table S3 reports the charge specific capacity and coulombic efficiency (CE) values during the first five cycles. The slight increase in capacity along the first 3–4 cycles observed for the VS-1200 and VS-1400 HCs can be explained by diffusion limitations during desodiation (i.e., release of Na ions from electrode's bulk was not fast enough) resulting from low or even negligible ultra/microporosity.

To assess the rate capability of the produced HC, five galvanostatic cycles at different current densities were performed using a two-electrode setup. As shown in Figure 7(a), when the current density was increased, the performance of the VS-1000, VS-1200 (the best-performing HC at the lowest current rate) and VS-1400 HCs decreased suddenly due to the slow kinetics of the intercalation processes. At current densities of 0.1 A g^{-1} or higher the best-performing carbon was VS-800 (delivering specific reversible charge capacities of 200, 168, 126, 67, and 39 mAh g^{-1} at 0.03 , 0.06 , 0.1 , 0.5 , and 1 A g^{-1} , respectively), as a consequence of its intrinsic larger pseudocapacitive contribution. Therefore, given the limited ion diffusion rate during intercalation, the major slope contribution of the VS-800 carbon makes it the best candidate for working at high current rates. Moreover, the relatively high micropore and ultramicropore volumes available in the VS-800 HC could provide fast channels for diffusion of Na ions to intercalation active sites and direct storage sites via pore filling. Tables S4 and S5 display the full results for reversible capacities referred to the active material mass and the electrode area, respectively.

After 25 discharge/charge cycles at various current rates, 5 additional cycles at the initial current density (0.03 A g^{-1}) were carried out. From the results shown in Figure 7(a), it can be seen that similar charge capacities were achieved, indicating a good stability of active materials when high currents were applied. In order to check the cycling stability of the VS-1200

HC, 315 discharge-charge cycles at 0.1 A g^{-1} were performed after 5 starting cycles at 0.03 A g^{-1} . The resulting charge capacities plotted in Figure 7b showed a downward trend with a sawtooth pattern, the latter being probably explained by certain diffusion limitations during desodiation, as already explained above. After the 315 cycles, when the current rate was set to its initial value (0.03 A g^{-1}), almost the same initial reversible charge capacity was retained (97%), indicating an excellent cycling stability of the VS-1200 HC-based electrode. The robust stability of the assembled anode was also confirmed by conducting 1000 cycles at a current rate of 1 A g^{-1} (see Figure S16a), achieving the same retention capacity of ca. 97% upon returning to 0.03 A g^{-1} . To assess the structural stability of the VS-1200 material, a cross-sectional view of the cycled anode was captured using SEM (see Figure S16 b–e). In spite of the formation of the solid electrolyte interface (SEI), neither fractures in the carbon matrix nor significant alterations in the morphology of the anode were observed. The noteworthy stability of the VS-1200 material is further confirmed when its performance is compared with that of other previously reported biomass-derived HCs (see Table S6).

The apparent diffusion coefficients (D_{Na^+}) for both sodiation and desodiation processes, which were calculated from GITT measurements (the electrode was previously subjected to three CV scans to allow the formation of the SEI layer), are shown in Figure 7(c) and (d), respectively (see also Tables S7–S11 for both

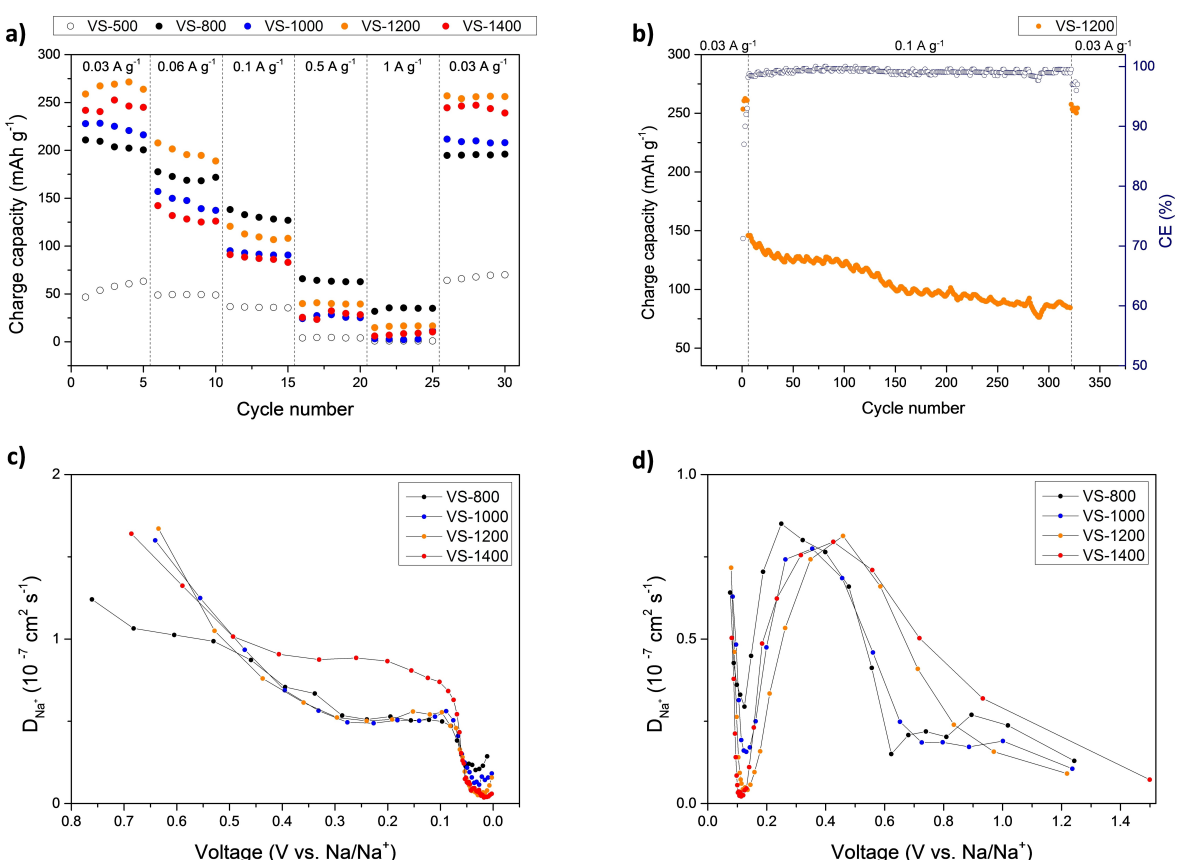


Figure 7. a) Charge specific capacities at various current densities ranging from 0.03 to 1 A g^{-1} , b) cycling performance of VS-1200 for 315 cycles at 0.1 A g^{-1} , and D_{Na^+} values calculated from GITT measurements along c) sodiation and d) desodiation.

D_{Na^+} and $\log D_{\text{Na}^+}$ values). From Figure 7(c) (sodiation), three stages related to different sodiation mechanisms can be observed along the voltage profile in line with the three-stage model suggested in the literature.^[28] A first stage taking place above 0.1 V with fast kinetics can be attributed to surface adsorption phenomena. Then, the sudden decrease in the apparent diffusion coefficients at ca. 0.1 V could be ascribed to intercalation processes. Finally, a third stage with slightly faster diffusion, and related to micropores and ultramicropores filling with Na ions, is detected. The fact that the increase in the D_{Na^+} values, in this third stage, was significantly higher for the VS-1200 HC in comparison with the VS-1400 one, is consistent with the textural features of both materials discussed above. Regarding the desodiation process (Figure 7d), the observed negative peak ca. 0.12 V might be ascribed to deintercalation processes. The fact that the lowest D_{Na^+} values were found for the most ordered carbons (VS-1200 and VS-1400) was expected, since their smaller mean interlayer spacing result in higher diffusion resistance. On the other hand, two small positive peaks appeared at ca. 0.75 and 0.90 V during desodiation of the VS-800 HC, and, to a lesser extent, VS-1000 HC. This slight improvement could be related to the desorption of Na ions from some surface functional groups.

To assess the influence of the acid-washing step on the electrochemical performance of the resulting anodes, the VS-500-UW intermediate char was carbonized up to 1200 °C. The performance of the resulting VS-1200-UW HC using a 2-electrode setup is compared with that of the VS-1200 HC in

Figure 8a, which clearly reveals that the unwashed HC performed worse, exhibiting significant lower charge capacities at all the tested current rates. The CO_2 adsorption isotherm of the VS-1200-UW carbon (given in Figure S17) revealed that this material retained a certain microporosity – in any case, greater than that of washed VS-1200 HC, as listed in Table 3 – despite the high carbonization temperature applied. This could be attributed to the catalytic effect of alkali and alkaline-Earth metals, which could probably enhanced decomposition of lignin during the second carbonization step, resulting in a greater microporosity development due to the emission of gaseous products and even char activation reactions.^[58–60] From the pattern of the apparent diffusion coefficients (during desodiation) shown in Figure 8b, it can be deduced a faster adsorption phenomenon in the slope region and the lack of storage through pore filling (at very low voltages), suggesting the possible occurrence of parasitic reactions involving the main inorganic components (Ca, K, Si, and Mg), which could act as ionic and/or electronic insulators on the carbon surfaces, hindering the pore-filling sodiation process.^[61–63] It is therefore proven that the removal of inorganic species by acid washing is highly recommended to improve the reversible capacity of vine shoots-derived HCs.

To provide further insights on the effect of using a simplified two-electrode setup instead of a three-electrode one, Figure 8(c) compares the charge capacities measured for the VS-1200 HC. When a low current density was applied (0.03 A g^{-1}) no evident differences between the two setups

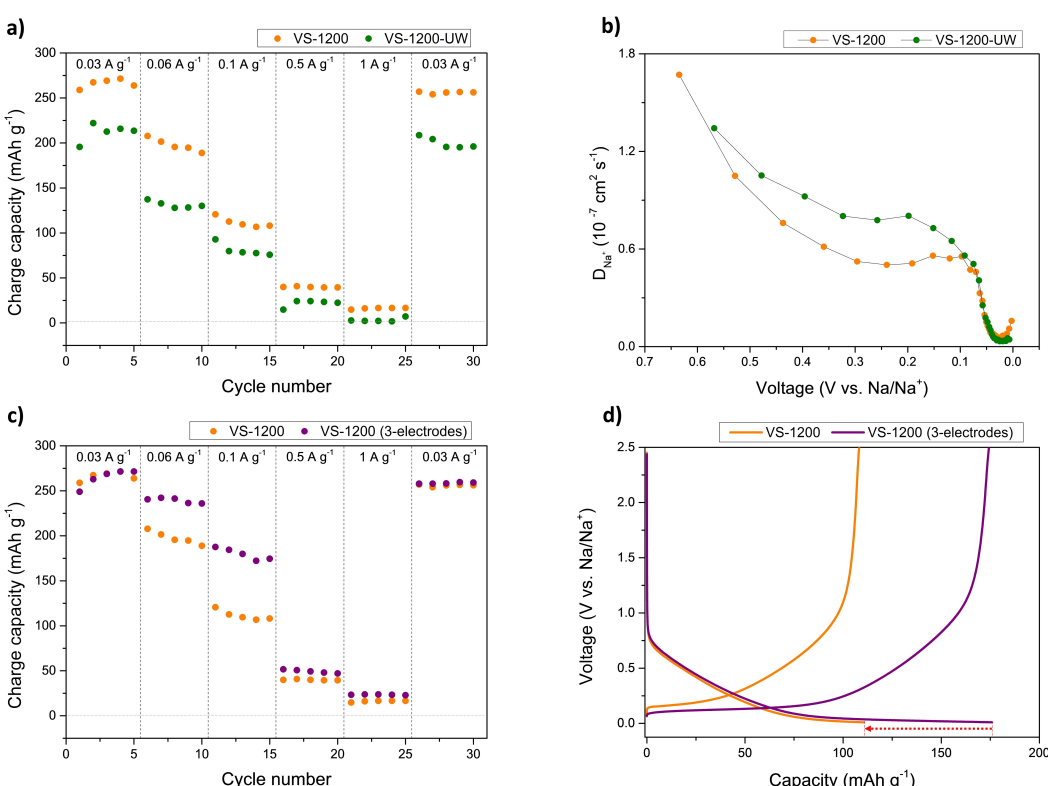


Figure 8. Influence of the acid-washing procedure on a) the rate capability and b) the D_{Na^+} values of VS-1200 and VS-1200-UW HCs; c) influence of using a third electrode (RE) in the rate capability of VS-1200; and d) galvanostatic cycling profile at 0.1 A g^{-1} for the VS-1200 HC using two- and three-electrode setups.

were found. However, when the galvanostatic discharge-charge cycling was performed at 0.06 and 0.1 Ag^{-1} , the use of a two-electrode cell resulted in a clear underestimation of capacity, which was of ca. 38% at 0.1 Ag^{-1} . The polarization of the metallic sodium counter electrode (CE) is attributed to the development of a passivation layer on its surface during the discharge process.^[64] At high current rates, even a slight overpotential at the sodium CE/RE is expected to cause the half-cells to reach the lower cutoff potential prematurely, thereby hindering the full sodiation of the hard carbon electrode. From Figure 8(d), which illustrates the CE/RE polarization effect during the discharge-charge profile at 0.1 Ag^{-1} , it can be observed how the use of a two-electrode setup led to a large systematic error when measuring the plateau contribution. This error is mitigated at higher intensities (0.5 and 1 Ag^{-1}) since the plateau contribution derived from the sodium intercalation phenomena was almost negligible at such current rates (see Figure S18).

Conclusions

An environmentally friendly and low-cost HC material was synthesized via a simple two-step carbonization approach (pyrolysis plus further carbonization), which included an acid-washing step previous to the second carbonization. Vine shoots have proven to be a good precursor for this purpose, facilitating their valorization into value-added active materials for large-scale electrochemical energy storage. The best-performing highest carbonization temperature was 1200 °C as a suitable balance was achieved between the growth of pseudographitic domains and the retention of microporosity and surface functional groups. The VS-1200 HC delivered a high reversible capacity (270 mAh g^{-1} at 0.03 Ag^{-1}), a more than acceptable ICE of 71%, and an impressive cycling stability (97% capacity retention after 315 cycles at 0.1 Ag^{-1}). This performance is comparable to that reported in the literature for other woody biomass-derived HCs synthesized at 1400 °C, with reversible capacities in the range of 226–337 mAh g^{-1} at 0.03 Ag^{-1} .^[16,43,65,66] The three-stage mechanism consisting in adsorption, intercalation, and pore filling was also corroborated from combined GITT measurements and textural characterization outcomes. It is noteworthy that the specific capacity was clearly underestimated when the simplified (and commonly employed) two-electrode half-cell setup was used, due to the polarization of the sodium metal counter/reference electrode. At a current density of 0.1 Ag^{-1} , a charge specific capacity of only 108 mAh g^{-1} (38% lower than that measured using a three-electrode cell) was obtained. Hence, we strongly suggest the use of three-electrode half-cell setups to assess the rate capability of active materials having a significant plateau contribution. Moreover, the observed diffusion limitations of the electrodes studied here at relatively high current rates encourage further research on alternative or complementary activation and/or heteroatom-doping treatments to enhance the transport of sodium ions and create new active sites on the surface of the electrode material.

Acknowledgements

This work is part of the research projects PID2019-107737RB-I00 and PID2021-127847OB-I00, funded by MCIN/AEI/10.13039/501100011033. The second project is also funded by “ERDF A way of making Europe”, by the European Union. The authors also acknowledge the funding from the Aragon Government (Ref. T22_23R). DA also acknowledges the funding from the Regional Government of Aragon (Spain) with a grant for postgraduate research contracts (2019–2023). LMA-ELECM and NANBIOSIS ICTs are gratefully acknowledged.

Conflict of Interests

The authors declare no conflict of interest.

Data Availability Statement

The data that support the findings of this study are available on request from the corresponding author. The data are not publicly available due to privacy or ethical restrictions.

Keywords: sodium-ion battery · vine shoots · hard carbon · interlayer spacing · polarization effect

- [1] F. Trotta, G. J. Wang, Z. Guo, Z. Xu, M. Crespo Ribadeneyra, H. Au, J. S. Edge, M. M. Titirici, L. Lander, *Adv. Sustainable Syst.* **2022**, *6*, 2200047.
- [2] U. Mittal, L. Djuandhi, N. Sharma, H. L. Andersen, *J. Phys. Energy* **2022**, *4*, 042001.
- [3] O. Lenchuk, P. Adelhelm, D. Mollenhauer, *Phys. Chem. Chem. Phys.* **2019**, *21*, 19378–19390.
- [4] W. Shao, H. Shi, X. Jian, Z.-S. Wu, F. Hu, *Adv. Energy Sustain. Res.* **2022**, *3*, 2200009.
- [5] A. V. Baskar, G. Singh, A. M. Ruban, J. M. Davidraj, R. Bahadur, P. Sooriyakumar, P. Kumar, A. Karakoti, J. Yi, A. Vinu, *Adv. Funct. Mater.* **2023**, *33*, 2208349.
- [6] L. Bottoni, H. Darjazi, L. Sbrascini, A. Staffolani, S. Gabrielli, G. Pastore, A. Tombesi, F. Nobili, *ChemElectroChem* **2023**, DOI 10.1002/CELC.202201117.
- [7] E. M. Lotfabad, J. Ding, K. Cui, A. Kohandehghan, W. P. Kalisvaart, M. Hazelton, D. Mitlin, *ACS Nano* **2014**, *8*, 7115–7129.
- [8] X. Li, X. Zeng, T. Ren, J. Zhao, Z. Zhu, S. Sun, Y. Zhang, *J. Alloys Compd.* **2019**, *787*, 229–238.
- [9] M. K. Rybarczyk, Y. Li, M. Qiao, Y. S. Hu, M. M. Titirici, M. Lieder, *J. Energy Chem.* **2019**, *29*, 17–22.
- [10] H. Y. Hu, Y. Xiao, W. Ling, Y. B. Wu, P. Wang, S. J. Tan, Y. S. Xu, Y. J. Guo, W. P. Chen, R. R. Tang, X. X. Zeng, Y. X. Yin, X. W. Wu, *Energy Technol.* **2021**, *9*, 1–7.
- [11] A. Baldinelli, X. Dou, D. Buchholz, M. Marinaro, S. Passerini, L. Barelli, *Green Chem.* **2018**, *20*, 1527–1537.
- [12] X. Dou, I. Hasa, D. Saurel, M. Jauregui, D. Buchholz, T. Rojo, S. Passerini, *ChemSusChem* **2018**, *11*, 3276–3285.
- [13] D. Qin, S. Chen, *J. Solid State Electrochem.* **2017**, *21*, 1305–1312.
- [14] J. Zhu, Y. Shan, T. Wang, H. Sun, Z. Zhao, L. Mei, Z. Fan, Z. Xu, I. Shakir, Y. Huang, B. Lu, X. Duan, *Nat. Commun.* **2016**, *7*, 13432.
- [15] W. Chen, M. Wan, Q. Liu, X. Xiong, F. Yu, Y. Huang, *Small Methods* **2019**, *3*, 1800323.
- [16] C. del M. Saavedra Rios, V. Simone, L. Simonin, S. Martinet, C. Dupont, *Biomass Bioenergy* **2018**, *117*, 32–37.
- [17] X. Dou, I. Hasa, D. Saurel, C. Vaalma, L. Wu, D. Buchholz, D. Bresser, S. Komaba, S. Passerini, *Mater. Today* **2019**, *23*, 87–104.

- [18] I. Hasa, S. Mariyappan, D. Saurel, P. Adelhelm, A. Y. Koposov, C. Masquelier, L. Croguennec, M. Casas-Cabanas, *J. Power Sources* **2021**, *482*, 228872.
- [19] X. Meng, P. E. Savage, D. Deng, *Environ. Sci. Technol.* **2015**, *49*, 12543–12550.
- [20] Z. E. Yu, Y. Lyu, Y. Wang, S. Xu, H. Cheng, X. Mu, J. Chu, R. Chen, Y. Liu, B. Guo, *Chem. Commun.* **2020**, *56*, 778–781.
- [21] V. Selvamani, R. Ravikumar, V. Suryanarayanan, D. Velayutham, S. Gopukumar, *Electrochim. Acta* **2016**, *190*, 337–345.
- [22] Y. Zhang, X. Li, P. Dong, G. Wu, J. Xiao, X. Zeng, Y. Zhang, X. Sun, *ACS Appl. Mater. Interfaces* **2018**, *10*, 42796–42803.
- [23] Y. Zhu, M. Chen, Q. Li, C. Yuan, C. Wang, *Carbon* **2018**, *129*, 695–701.
- [24] M. Poletto, A. J. Zattera, M. M. C. Forte, R. M. C. Santana, *Bioresour. Technol.* **2012**, *109*, 148–153.
- [25] P. C. Rath, J. Patra, H. Huang, D. Bresser, T. Wu, J. Chang, *ChemSusChem* **2019**, *12*, 2302–2309.
- [26] D. A. Stevens, J. R. Dahn, *J. Electrochem. Soc.* **2000**, *147*, 1271.
- [27] Y. Cao, L. Xiao, M. L. Sushko, W. Wang, B. Schwenzer, J. Xiao, Z. Nie, L. V. Saraf, Z. Yang, J. Liu, *Nano Lett.* **2012**, *12*, 3783–3787.
- [28] C. Bommier, T. W. Surta, M. Dolgos, X. Ji, *Nano Lett.* **2015**, *15*, 5888–5892.
- [29] S. Alvin, D. Yoon, C. Chandra, H. S. Cahyadi, J. H. Park, W. Chang, K. Y. Chung, J. Kim, *Carbon* **2019**, *145*, 67–81.
- [30] N. Sun, Z. Guan, Y. Liu, Y. Cao, Q. Zhu, H. Liu, Z. Wang, P. Zhang, B. Xu, *Adv. Energy Mater.* **2019**, *9*, 1901351.
- [31] B. Zhang, C. M. Ghimbeu, C. Laberty, C. Vix-Guterl, J. M. Tarascon, *Adv. Energy Mater.* **2016**, *6*, 1–9.
- [32] D. Alvira, D. Antorán, J. J. Manyà, *Chem. Eng. J.* **2022**, *447*, 137468.
- [33] P. Yu, W. Tang, F.-F. Wu, C. Zhang, H.-Y. Luo, H. Liu, Z.-G. Wang, *Rare Met.* **2020**, *39*, 1019–1033.
- [34] Y. Zheng, Y. Lu, X. Qi, Y. Wang, L. Mu, Y. Li, Q. Ma, J. Li, Y. S. Hu, *Energy Storage Mater.* **2019**, *18*, 269–279.
- [35] J. Yang, X. Wang, W. Dai, X. Lian, X. Cui, W. Zhang, K. Zhang, M. Lin, R. Zou, K. P. Loh, Q.-H. Yang, W. Chen, *Nano-Micro Lett.* **2021**, *13*, 98.
- [36] L. Jiménez, V. Angulo, E. Ramos, M. J. De la Torre, J. L. Ferrer, *Ind. Crops Prod.* **2006**, *23*, 122–130.
- [37] M. Videgain-Marco, P. Marco-Montori, C. Martí-Dalmau, M. del Carmen Jaizme-Vega, J. J. Manyà-Cervelló, F. J. García-Ramos, *Agronomy* **2020**, *10*, 104.
- [38] W.-J. Liu, H. Jiang, H.-Q. Yu, *Chem. Rev.* **2015**, *115*, 12251–12285.
- [39] J. J. Manyà, D. Alvira, M. Videgain, G. Duman, J. Yanik, *Energy Fuels* **2021**, *35*, 3174–3185.
- [40] D. Alvira, D. Antorán, J. J. Manyà, *J. Energy Chem.* **2022**, *75*, 457–477.
- [41] L. G. Cançado, K. Takai, T. Enoki, M. Endo, Y. A. Kim, H. Mizusaki, A. Jorio, L. N. Coelho, R. Magalhães-Paniago, M. A. Pimenta, *Appl. Phys. Lett.* **2006**, *88*, 163106.
- [42] X. Dou, I. Hasa, M. Hekmatfar, T. Diemant, R. J. Behm, D. Buchholz, S. Passerini, *ChemSusChem* **2017**, *10*, 2668–2676.
- [43] C. del Mar Saavedra Rios, L. Simonin, C. M. Ghimbeu, C. Vaulot, D. da Silva Perez, C. Dupont, *Fuel Process. Technol.* **2022**, *231*, 107223.
- [44] C. Nita, B. Zhang, J. Dentzer, C. Matei Ghimbeu, *J. Energy Chem.* **2021**, *58*, 207–218.
- [45] T. Zhang, J. Mao, X. Liu, M. Xuan, K. Bi, X. L. Zhang, J. Hu, J. Fan, S. Chen, G. Shao, *RSC Adv.* **2017**, *7*, 41504–41511.
- [46] L. Zhao, Z. Hu, W. Lai, Y. Tao, J. Peng, Z. Miao, Y. Wang, S. Chou, H. Liu, S. Dou, *Adv. Energy Mater.* **2021**, *11*, 2002704.
- [47] S. Alvin, D. Yoon, C. Chandra, R. F. Susanti, W. Chang, C. Ryu, J. Kim, *J. Power Sources* **2019**, *430*, 157–168.
- [48] S. Alvin, C. Chandra, J. Kim, *Chem. Eng. J.* **2021**, *411*, 128490.
- [49] L. Burhenne, J. Messmer, T. Aicher, M.-P. Laborie, *J. Anal. Appl. Pyrolysis* **2013**, *101*, 177–184.
- [50] J. Deng, T. Xiong, H. Wang, A. Zheng, Y. Wang, *ACS Sustainable Chem. Eng.* **2016**, *4*, 3750–3756.
- [51] W. Zhang, S. Wei, P. Bai, W. Liu, C. Yang, L. Xu, *Appl. Catal. B* **2023**, *325*, 122391.
- [52] K. Kim, D. G. Lim, C. W. Han, S. Osswald, V. Ortalan, J. P. Youngblood, V. G. Pol, *ACS Sustainable Chem. Eng.* **2017**, *5*, 8720–8728.
- [53] K. Zeng, R. Li, D. P. Minh, E. Weiss-Hortala, A. Nzihou, D. Zhong, G. Flamant, *Energy* **2020**, *206*, 118128.
- [54] K. Stańczyk, R. Dziembaj, Z. Piwowarska, S. Witkowski, *Carbon* **1995**, *33*, 1383–1392.
- [55] D. Su, M. Huang, J. Zhang, X. Guo, J. Chen, Y. Xue, A. Yuan, Q. Kong, *Nano Res.* **2020**, *13*, 2862–2868.
- [56] Y. Li, M. Chen, B. Liu, Y. Zhang, X. Liang, X. Xia, *Adv. Energy Mater.* **2020**, *10*, 2000927.
- [57] M. Wahid, Y. Gawli, D. Puthusseri, A. Kumar, M. V. Shelke, S. Ogale, *ACS Omega* **2017**, *2*, 3601–3609.
- [58] S. Wang, Z. Li, X. Bai, W. Yi, P. Fu, *Bioresour. Technol.* **2018**, *268*, 323–331.
- [59] A. Nzihou, B. Stanmore, N. Lyczko, D. P. Minh, *Energy* **2019**, *170*, 326–337.
- [60] C. Matei Ghimbeu, B. Zhang, A. Martinez de Yuso, B. Réty, J.-M. Tarascon, *Carbon* **2019**, *153*, 634–647.
- [61] A. Beda, J.-M. Le Meins, P.-L. Taberna, P. Simon, C. Matei Ghimbeu, *Sustain. Mater. Technol.* **2020**, *26*, e00227.
- [62] C. del Mar Saavedra Rios, L. Simonin, A. de Geyer, C. Matei Ghimbeu, C. Dupont, *Energies* **2020**, *13*, 3513.
- [63] J. Conder, C. Vaulot, C. Marino, C. Villevieille, C. M. Ghimbeu, *ACS Appl. Energ. Mater.* **2019**, *2*, 4841–4852.
- [64] A. Rudola, D. Aurbach, P. Balaya, *Electrochim. Commun.* **2014**, *46*, 56–59.
- [65] K. Nakabayashi, H. Yi, D.-Y. Ryu, D. Chung, J. Miyawaki, S.-H. Yoon, *Chem. Lett.* **2019**, *48*, 753–755.
- [66] Y. Wang, Z. Feng, W. Zhu, V. Gariépy, C. Gagnon, M. Provencher, D. Laul, R. Veillette, M. Trudeau, A. Guerfi, K. Zaghib, *Materials* **2018**, *11*, 1294.

Manuscript received: June 1, 2023

Revised manuscript received: August 1, 2023

Accepted manuscript online: August 2, 2023

Version of record online: August 10, 2023